DINAME 2023 - Proceedings of the XIX International Symposium on Dynamic Problems of Mechanics,
A.S. De Paula, A.T. Fabro and M.R. Machado (Editors), ABCM.
Pirenópolis, Go, Brazil, February 26th to March 3rd, 2023

Flexural wave propagation in metamaterial beams with beam-type resonators and eddy current damping

Matheus Basílio Rodrigues Fernandes[1], **Thiago de Paula Sales**[1], **and Domingos Alves Rade**[1]

[1] Aeronautics Institute of Technology, Mechanical Engineering Division
Praça Mal. Eduardo Gomes, 50, São José dos Campos, SP, Brazil

Abstract: It is well known from the literature that the vibration attenuation achieved in finite metamaterials increases as the number of unit cells increases. This leads to more natural frequencies within a given pass-band and, due to the periodicity of the dispersion diagram, they tend to cluster at its boundaries. This can be problematic, since in a narrow frequency range encompassing the end of an attenuation band and the beginning of a pass-band, one can move from a highly attenuated region to a region with large vibration transmissibility. In this context, this paper considers the use of localized eddy current-based dampers (ECDs) to enhance the attenuation performance of regions with a high density of natural frequencies. The effects of system parameters on the dispersion diagram and vibration transmissibility are investigated. The results show that ECDs are able to increase the vibration attenuation of metamaterial beams with beam-type resonators.

Keywords: elastic metamaterials, local resonators, eddy current damping

INTRODUCTION

Acoustic and elastic metamaterials are periodic structures designed so that they exhibit properties not found in natural materials, such as negative effective density (Yao et al., 2008), elastic modulus (Liu et al., 2000) or both (Cheng et al., 2008). Contrary to what occurs in phononic crystals, in metamaterials, bandgaps occur at wavelengths that are not associated with the dimensions of the unit cell, but with the resonance frequency of the internal oscillators. This makes them quite attractive, as bandgaps can be generated at frequencies that are in principle arbitrarily low.

Although a huge variety of different metamaterial designs have been proposed and studied, most investigations focus on structures without any dissipation mechanisms, so that the obtained vibration attenuation characteristics are due only to the local resonance phenomenon (or Bragg scattering, for phononic crystals). This is mainly due to the greater ease of modeling and interpretation of results for undamped structures, not to mention that weakly damped structures are usually well approximated by the associated conservative model. The fact is that all real structures present some degree of damping, and its consideration in the mathematical model can lead to at least two benefits. First, taking damping into account can lead to changes in the band structure and transmission spectrum, allowing for a better representative model of the real underlying system. Second, damping can be wisely introduced in the structure to, in conjunction with periodicity, obtain increased vibration attenuation performance.

Part of the existing work in the literature regarding damped phononic crystals and metamaterials focuses on efficient and reliable numerical techniques to characterize the influence of different damping models (like viscous or viscoelastic) on the dispersion diagram of periodic structures. In this sense, they can be classified based on the type of solution that is sought (Andreassen and Jensen, 2013; Frazier and Hussein, 2016; Hussein et al., 2014). One class of methods searches for a band structure by means of a formulation $k = k(\omega)$, restricting ω (the circular frequency) to real values and allowing k (the wavenumber) to be complex, such that the dissipation can be observed only spatially, following the imaginary part of k. These cases are commonly referred to as harmonic wave propagation, and they have direct correspondence to experimental situations in which a structure is subjected to a forced harmonic excitation. Another class looks for solutions of the form $\omega = \omega(k)$, with k being real and allowing ω to be complex. In this case, dissipation effects are observed through temporal rather than spatial attenuation. This type of formulation, which is referred to as free wave propagation, corresponds directly to experimental problems with wave generation due to an initial disturbance, or in forced cases in which the loading is, for example, impulsive. Andreassen and Jensen (2013) applied both formulations in the study of a 2D phononic crystal and showed that the dispersion diagram and the temporal rate of decay of the wave amplitude predicted by both methods agree well for small amounts of damping, but begin to diverge as it increases, especially for short wavelengths. It is worth mentioning that recent efforts (Frazier and Hussein, 2016) have sought to construct a band diagram with simultaneously complex frequency and wavenumber, but, until now, with applications restricted to discrete systems, and with few degrees of freedom.

Regarding structures with internal oscillators, Hussein and Frazier (2013), studying discrete diatomic and mass-in-mass systems, coined the term *metadamping* to designate the phenomenon of damping emergence due to the presence of internal oscillators in metamaterials, which causes them to have a higher damping ratio than statically equivalent phononic crystals. Also, several researches have investigated the influence of different damping models in the most varied configurations of metamaterials, studying the role of damping separately in the host structure and in the internal resonator. The effects of structural damping on a 2D metamaterial made by adding a resonant structure in the form of a clamped beam to a flat plate were investigated, both numerically and experimentally, by Belle et al. (2017). Their findings showed that damping in the resonators mainly affects the frequency range in and around the bandgap, while damping in the host structure primarily influences the pass-band region. Considering a free wave propagation approach, Aladwani and Nouh (2020a) studied, through the frequency-damping band diagram, the influence of damping on different parts of a metamaterial beam with lumped resonators. They showed that damping in the resonator increases the modal damping ratio in regions close to the bandgap and that, when added to the host beam, damping can suppress the beneficial effect triggered by the resonator damping around the bandgap edges. In a related work (Aladwani and Nouh, 2020b), the same authors considered a fiber-reinforced composite beam with multiple discrete resonators connected in series to study the influence of the position of the viscoelastic damping on the structure. They reported that the placement position of viscoelastic inserts in the resonant structure dictates whether a higher damping ratio will be obtained near the boundaries of the bandgaps, or in the pass-band between them. Regarding longitudinal waves, a bi-material rod with internal resonators was considered by Lou et al. (2018), who showed that dissipation in the host material and in the resonators can lead to the coalescence of Bragg and appropriately tuned local resonance (LR) bandgaps, forming a single, wider bandgap. They found, however, that damping in the internal resonator has little effect on Bragg bandgaps.

In addition to the selection of geometric and material parameters, which unequivocally determine the wave propagation characteristics of the infinite structure, a key aspect in the design of phononic crystals and metamaterials is the choice of the number of unit cells to be considered. Of course, all real structures are finite in size, and so the infinite-cell Bloch model is just an approximation of the associated finite-sized real structure. In general, an increase in the number of unit cells leads to an improvement in the vibration attenuation, at the price of increasing the number of natural frequencies of the finite system within a given branch in the pass-band (Mace, 2014). Furthermore, it is known (Mace, 2014) that the natural frequencies of the finite system tend to cluster close to the boundaries of the pass-bands. This is due to the periodicity of the dispersion diagram in the k-space, which causes $\partial \omega / \partial k = 0$ at the boundary between a pass-band and a stop-band. This can be problematic, since in a narrow frequency range which encompasses the end of a given attenuation band and the beginning of the corresponding pass-band, one can move from a highly attenuated region to a region with large vibration transmissibility.

Within this framework, this work proposes the use of eddy current (EC) damping to improve the attenuation performance of these frequency ranges with high density of natural frequencies. EC damping arises due to the variation of the magnetic flux through the surface of a conductor, which can occur, e.g., due to relative motion between a permanent magnet (PM) and a metallic conductor. According to Faraday's law, the variation of the magnetic flux generates an electromotive force (emf) in the conductor, which leads to the appearance of an electric current in it, which, in turn, induces another magnetic field that opposes the first one (obeying Lenz's law). The interaction between the induced magnetic field and that of the PM leads to the emergence of a resistive force to motion that, as shown later, is modeled to be proportional to the relative velocity between the conductor and the PM. In the literature, works are found reporting that damping based on ECs has proven effective in suppressing vibrations in structures such as beams (Sodano et al., 2006), plates (Bae et al., 2018), multi-storey frames (Ao and Reynolds, 2019), and turbine blades (Laborenz et al., 2012). EC-based damping is interesting in the sense that it allows the introduction of damping at localized points in the structure, without greatly affecting the tuning of resonators. In addition, it has advantages such as the possibility of changing the damping level after installation, and the absence of mechanical contact between the PM and the conductive metal.

The remainder of this paper is organized as follows. First, the mathematical modeling of the metamaterial beam with EC dampers is presented: the spectral element method (SEM) modeling of a Timoshenko beam is initially presented, which is followed by the modeling of the beam-type resonators. Later, one addresses the computation of the dispersion diagram of the infinite system and the forced response of the associated finite structure. Numerical results are reported afterward: first, the trade-off between vibration attenuation and its robustness in a finite metamaterial is presented, and, then, the use of EC damping in metamaterial beams with beam-type resonators is stressed. Concluding remarks are provided at last.

METAMATERIAL BEAM MODELING

The system under study is shown in Fig. 1. It consists of a host beam, to which resonant structures are rigidly connected in a periodic arrangement. Each resonator is comprised of a double cantilever beam with a thin copper sheet attached to its surface. The flux of the magnetic fields, generated by nearby PMs, through the copper sheets varies as the resonator oscillates, generating ECs in the copper conductor, which in turn leads to the emergence of damping forces in the resonators. Metamaterial beams with similar beam-type resonators have been investigated in other studies (El-Borgi et al., 2020; Serrano et al., 2019; Xiao et al., 2013), but little attention has been devoted to the influence of resonator damping on the wave propagation and vibration attenuation performance. Here, we explore how a concentrated damping element generated by ECs can be exploited to improve the attenuation performance of metamaterial beams with beam-type resonators. The model for computing the damping forces that arise due to ECs is presented below. Since the unit cell shown in Fig. 1 is composed by beam-like structures, the main aspects related to the modeling of Timoshenko beams through the SEM are briefly revisited.

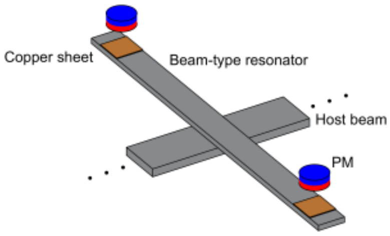

Figure 1 – Schematic diagram of the unit cell under study.

Model for the eddy current damping force

The magnetic induction field created by a cylindrical PM having an axial polarization can be found by using the equivalence between the coulombian approach and the amperian current model (Ravaud et al., 2010). If J is the axial polarization of the PM, R_{PM} its radius and L_{PM} its length, this field can be written, in cylindrical coordinates, as (Ravaud et al., 2010):

$$B_r(r,z) = J/(2\pi)\cdot\mathbf{C}_{\mathrm{a}}, \qquad B_z(r,z) = J/(2\pi)\cdot\mathbf{C}_{\mathrm{b}}, \tag{1}$$

where r and z are cylindrical coordinates,

$$\begin{aligned}\mathbf{C}_{\mathrm{a}} &= \sum\nolimits_{i=1}^{2}(-1)^{i}\left\{a_i/\left(r\sqrt{\alpha_i}\right)\cdot\mathbf{K}\left[-2b/\alpha_i\right]-\sqrt{\alpha_i}/r\cdot\mathbf{E}\left[-2b/\alpha_i\right]\right\},\\ \mathbf{C}_{\mathrm{b}} &= \sum\nolimits_{i=1}^{2}(-1)^{i}\epsilon_{4,i}\left\{(cr-bR_{\mathrm{PM}})\left(\mathbf{\Pi}\left[\epsilon_{1,i},\epsilon_{3,i},\epsilon_{2,i}\right]+\mathbf{\Pi}\left[\epsilon_{1,i},\epsilon_{2,i}\right]\right)+(bR_{\mathrm{PM}}-a_i r)\left(\mathbf{F}\left[\epsilon_{3,i},\epsilon_{2,i}\right]+\mathbf{K}\left[\epsilon_{2,i}\right]\right)\right\},\end{aligned} \tag{2}$$

and:

$$\alpha_i = (r-R_{\mathrm{PM}})^2+(z-z_i)^2, \quad \epsilon_{1,i}=\frac{(a_i-c)}{(a_i+b)}, \quad \epsilon_{2,i}=\frac{(a_i-b)}{(a_i+b)}, \quad \epsilon_{3,i}=-\arcsin\left[\frac{a_i+b}{a_i-b}\right], \quad \epsilon_{4,i}=\frac{2R_{\mathrm{PM}}(z-z_i)}{b(a_i-c)\sqrt{-a_i-b}},$$

$$a_i = r^2+R_{\mathrm{PM}}^2+(z-z_i)^2, \quad b=2rR_{\mathrm{PM}}, \quad c=r^2+R_{\mathrm{PM}}^2, \quad z_1=-L_{\mathrm{PM}}/2, \quad z_2=L_{\mathrm{PM}}/2. \tag{3}$$

In Eq. (2), $\mathbf{K}[m]$, $\mathbf{F}[\phi,m]$, $\mathbf{E}[m]$, $\mathbf{\Pi}[n,m]$, and $\mathbf{\Pi}[n,\phi,m]$ represent the following elliptic integrals:

$$\mathbf{K}[m]=\int_0^{\frac{\pi}{2}}\frac{1}{\sqrt{1-m\sin(\theta)^2}}d\theta, \qquad \mathbf{F}[\phi,m]=\int_0^{\phi}\frac{1}{\sqrt{1-m\sin(\theta)^2}}d\theta, \qquad \mathbf{E}[m]=\int_0^{\frac{\pi}{2}}\sqrt{1-m\sin(\theta)^2}d\theta,$$

$$\mathbf{\Pi}[n,\phi,m]=\int_0^{\phi}\frac{1}{\sqrt{1-n\sin(\theta)^2}}\frac{1}{\sqrt{1-m\sin(\theta)^2}}d\theta, \qquad \mathbf{\Pi}[n,m]=\mathbf{\Pi}\left[n,\frac{\pi}{2},m\right]. \tag{4}$$

If the surface charges are assumed to be ignored, the current density $\mathbf{J}$ induced in a conducting sheet with electrical conductivity σ, moving with velocity $\mathbf{v}$ perpendicularly to a magnetic induction field $\mathbf{B}$, is given by (Sodano et al., 2005):

$$\mathbf{J}=\sigma\left(\mathbf{v}\times\mathbf{B}\right). \tag{5}$$

Using Eqs. (5) and (1), the damping force due to the eddy current can be assessed using Lorentz force, as is given by (Sodano et al., 2005, 2006):

$$\mathbf{F}=\int_V \mathbf{J}\times\mathbf{B}\,\mathrm{d}V=-\mathbf{k}\sigma v\int_V B_r^2\,\mathrm{d}V, \tag{6}$$

from which the equivalent viscous damping coefficient due to the eddy currents can be calculated as:

$$c_{\mathrm{EC}}=\sigma\int_V B_r^2\,\mathrm{d}V. \tag{7}$$

The integration appearing in Eq. (7) must be performed over the entire volume of the conductive surface. In the present work, it is computed using a numerical integration method.

SEM modeling of a Timoshenko beam

The equations of motion for the free vibration of a uniform beam modeled according to Timoshenko's theory can be written as (Lee, 2009; Mei and Mace, 2005):

$$V'(x,t)=\rho A\ddot{w}(x,t), \qquad M'(x,t)+V(x,t)=\rho I\ddot{\phi}(x,t), \tag{8}$$

where the bending moment $M(x,t)$ and the transverse shear force $V(x,t)$ can be calculated as:

$$V(x,t) = \kappa GA\left(w'(x,t) - \phi(x,t)\right), \qquad M(x,t) = EI\phi'(x,t). \tag{9}$$

The constants E, G, ρ, A, I, κ denote the Young's modulus, shear modulus, mass density, cross-sectional area, second moment of area, and shear correction factor, respectively, and $w(x,t)$, and $\phi(x,t)$ are the transverse displacement, and slope, respectively. The dot ($\dot{}$) represents time derivatives, whereas the prime ($'$) denotes derivatives w.r.t. the spatial coordinate.

A propagating wave is assumed as the solution of Eq. (8):

$$w(x,t) = ae^{-i(kx-\omega t)}, \qquad \phi(x,t) = \beta ae^{-i(kx-\omega t)}, \tag{10}$$

where β is the modal ratio, k is the wavenumber, and ω is the circular frequency. Substituting Eq. (10) into Eq. (8) yields an eigenvalue problem, whose characteristic equation is given by:

$$(\kappa GAEI)\,k^4 - \left(\kappa GA\rho I\omega^2 + EI\rho A\omega^2\right)k^2 + \left(\rho I\omega^2 - \kappa GA\right)\rho A\omega^2 = 0. \tag{11}$$

Equation (11) is bi-quadratic in k, whose solutions k_i $(i = 1, \cdots, 4)$ are easily found as:

$$k_t \equiv k_1 = -k_2 = \frac{1}{\sqrt{2}}k_F\sqrt{\eta k_F^2 + \sqrt{\eta^2 k_F^4 + 4\left(1 - \eta_1 k_G^4\right)}} \qquad k_{\mathrm{e}} \equiv k_3 = -k_4 = \frac{1}{\sqrt{2}}k_F\sqrt{\eta k_F^2 - \sqrt{\eta^2 k_F^4 + 4\left(1 - \eta_1 k_G^4\right)}}, \tag{12}$$

where:

$$\eta_1 = \frac{I}{A}, \qquad \eta_2 = \frac{EI}{\kappa GA}, \qquad \eta = \eta_1 + \eta_2, \qquad k_F = \sqrt{\omega}\left(\frac{\rho A}{EI}\right)^{1/4}, \qquad k_G = \sqrt{\omega}\left(\frac{\rho}{\kappa G}\right)^{1/4}. \tag{13}$$

Furthermore, regarding the SEM, the 4 × 4 spectral element matrix, also called the exact dynamic stiffness matrix (DSM), for a homogeneous Timoshenko beam with length L can be expressed as (Lee, 2009):

$$S^{(e)}(\omega) = \begin{bmatrix} \mathbf{S}_{11} & \mathbf{S}_{12} \\ \mathbf{S}_{21} & \mathbf{S}_{22} \end{bmatrix} = EI\begin{bmatrix} s_{11} & s_{12} & s_{13} & s_{14} \\ s_{12} & s_{22} & s_{23} & s_{24} \\ s_{13} & s_{23} & s_{33} & s_{34} \\ s_{14} & s_{24} & s_{34} & s_{44} \end{bmatrix}. \tag{14}$$

Expressions for the components s_{ij} are omitted here for conciseness, being available elsewhere (Lee, 2009).

Modeling of the beam-type resonator

The global matrix equation for the unit cell, encompassing both the host beam and the beam-type resonators, can be obtained by assembling the spectral element matrices for each of these parts, in a completely analogous way to what is done in the conventional finite element method (FEM). Alternatively, the influence of the beam-type resonator can be incorporated considering its driving-point dynamic stiffness. For that, following the SEM, the equations of motion of the two waveguides that comprise the resonator (see Fig. 1) can be written as:

$$\begin{bmatrix} \mathbf{S}_{11}^{(1)} & \mathbf{S}_{12}^{(1)} & \mathbf{0} \\ \mathbf{S}_{21}^{(1)} & \mathbf{S}_{22}^{(1)} + \mathbf{S}_{11}^{(2)} + \mathbf{S}_{\mathrm{EC}} & \mathbf{S}_{12}^{(2)} \\ \mathbf{0} & \mathbf{S}_{21}^{(2)} & \mathbf{S}_{22}^{(2)} \end{bmatrix}\begin{Bmatrix} \mathbf{d}_1 \\ \mathbf{d}_2 \\ \mathbf{d}_3 \end{Bmatrix} = \begin{Bmatrix} \mathbf{f}_1 \\ \mathbf{f}_2 \\ \mathbf{f}_3 \end{Bmatrix}, \tag{15}$$

where:

$$\mathbf{d}_1 = \left\{W_1^{(r)} \quad 0\right\}^{\mathrm{T}}, \quad \mathbf{d}_2 = \left\{W_2^{(r)} \quad \Phi_2^{(r)}\right\}^{\mathrm{T}}, \quad \mathbf{d}_3 = \left\{W_3^{(r)} \quad \Phi_3^{(r)}\right\}^{\mathrm{T}}, \quad \mathbf{f}_1 = \left\{F_0 \quad 0\right\}^{\mathrm{T}}, \quad \mathbf{f}_2 = \mathbf{f}_3 = \left\{0 \quad 0\right\}^{\mathrm{T}}. \tag{16}$$

The matrix $\mathbf{S}_{\mathrm{EC}}$, which represents the contribution of the EC damper to the dynamic stiffness of the resonator, can be read as:

$$\mathbf{S}_{\mathrm{EC}} = \begin{bmatrix} S_{\mathrm{EC}} & 0 \\ 0 & 0 \end{bmatrix}, \qquad \text{where} \quad S_{\mathrm{EC}} = -\omega^2 m_{\mathrm{EC}} + i\omega c_{\mathrm{EC}}, \tag{17}$$

with m_{EC} and c_{EC} being, respectively, the mass of the copper sheet and the damping coefficient of the EC damper. The nodal degrees of freedom $(W_1^{(r)}, W_2^{(r)}, \Phi_2^{(r)}, W_3^{(r)}, \Phi_3^{(r)})$ can be found by solving Eq. (15), after applying the boundary conditions given by Eq. (16). Then, the driving-point dynamic stiffness of the resonator can be computed as:

$$S_{\mathrm{r}} = \frac{F_0}{W_1^{(r)}}. \tag{18}$$

The approach chosen here of condensing the resonator degrees of freedom through its driving-point dynamic stiffness, in addition to being exact, has the advantage of decreasing the computational cost associated with calculating both the dispersion diagram of the infinite system and the forced harmonic response of the truncated finite structure, which will be addressed later.

Computation of the dispersion diagram of the infinite system

To compute the dispersion diagram of the infinite periodic system, it is enough to consider a single unit cell. In the framework of the SEM, the equations of motion in the frequency domain for the unit cell shown in Fig. 1 can be compactly written as:

$$\begin{bmatrix} \mathbf{S}_{\mathrm{LL}} & \mathbf{S}_{\mathrm{LR}} \\ \mathbf{S}_{\mathrm{RL}} & \mathbf{S}_{\mathrm{RR}} \end{bmatrix} \begin{Bmatrix} \mathbf{d}_{\mathrm{L}} \\ \mathbf{d}_{\mathrm{R}} \end{Bmatrix} = \begin{Bmatrix} \mathbf{f}_{\mathrm{L}} \\ \mathbf{f}_{\mathrm{R}} \end{Bmatrix}, \tag{19}$$

where:

$$\mathbf{d}_{\mathrm{L}} = \{W_1 \quad \Phi_1\}^{\mathrm{T}}, \quad \mathbf{d}_{\mathrm{R}} = \{W_2 \quad \Phi_2\}^{\mathrm{T}}, \quad \mathbf{f}_{\mathrm{L}} = \{Q_1 \quad M_1\}^{\mathrm{T}}, \quad \mathbf{f}_{\mathrm{R}} = \{Q_2 \quad M_2\}^{\mathrm{T}}. \tag{20}$$

The subscripts L and R stand for the left and right nodes of the unit cell, respectively. The global DSM is assembled from the DSMs of the host beam and the resonator, and can be written as:

$$\begin{bmatrix} \mathbf{S}_{\mathrm{LL}} & \mathbf{S}_{\mathrm{LR}} \\ \mathbf{S}_{\mathrm{RL}} & \mathbf{S}_{\mathrm{RR}} \end{bmatrix} = \begin{bmatrix} \mathbf{S}_{11} + \mathbf{S}_{\mathrm{r}} & \mathbf{S}_{12} \\ \mathbf{S}_{21} & \mathbf{S}_{22} \end{bmatrix}, \qquad \text{where} \quad \mathbf{S}_{\mathrm{r}} = \begin{bmatrix} S_{\mathrm{r}} & 0 \\ 0 & 0 \end{bmatrix}, \tag{21}$$

with S_{r} given by Eq. (18). One remarks a similar procedure has been adopted by Xiao et al. (2013).

Equation (19) can be reorganized as follows, in order to obtain the transfer matrix (TM) $\mathbf{T}(\omega)$ of the unit cell:

$$\begin{Bmatrix} \mathbf{d}_{\mathrm{R}} \\ -\mathbf{f}_{\mathrm{R}} \end{Bmatrix} = \underbrace{\begin{bmatrix} -\mathbf{S}_{\mathrm{LR}}^{-1}\mathbf{S}_{\mathrm{LL}} & \mathbf{S}_{\mathrm{LR}}^{-1} \\ -\mathbf{S}_{\mathrm{RL}} + \mathbf{S}_{\mathrm{RR}}\mathbf{S}_{\mathrm{LR}}^{-1}\mathbf{S}_{\mathrm{LL}} & -\mathbf{S}_{\mathrm{RR}}\mathbf{S}_{\mathrm{LR}}^{-1} \end{bmatrix}}_{\mathbf{T}(\omega)} \begin{Bmatrix} \mathbf{d}_{\mathrm{L}} \\ \mathbf{f}_{\mathrm{L}} \end{Bmatrix}. \tag{22}$$

When considering wave propagation in infinite periodic systems, the state vectors associated with the left and right boundaries of the unit cell are related through the propagation constant μ by means of Bloch conditions, as follows (Hussein et al., 2014):

$$\begin{Bmatrix} \mathbf{d}_{\mathrm{R}} \\ -\mathbf{f}_{\mathrm{R}} \end{Bmatrix} = \mathrm{e}^{i\mu} \begin{Bmatrix} \mathbf{d}_{\mathrm{L}} \\ \mathbf{f}_{\mathrm{L}} \end{Bmatrix}, \tag{23}$$

which, upon substituting in Eq. (22), produces the following standard eigenvalue problem:

$$\mathbf{T}(\omega) \begin{Bmatrix} \mathbf{d}_{\mathrm{L}} \\ \mathbf{f}_{\mathrm{L}} \end{Bmatrix} = \mathrm{e}^{i\mu} \begin{Bmatrix} \mathbf{d}_{\mathrm{L}} \\ \mathbf{f}_{\mathrm{L}} \end{Bmatrix}. \tag{24}$$

Following the harmonic wave approach, the dispersion diagram is calculated by imposing a real frequency ω and solving the eigenvalue problem given by Eq. (24) in order to compute the propagation constant μ.

The nature of wave propagation depends on the value obtained for μ. Eigenvalues of the form $e^{i\alpha}$ ($\alpha \in \mathbb{R}$) are associated with propagating wave modes, while eigenvalues of the form $e^{\beta + i\alpha}$ ($\alpha, \beta \in \mathbb{R}$) relate to spatially-attenuated wave modes. Accordingly, for conservative systems, pass-bands are defined as the frequency regions where at least one wave mode exhibits a purely real propagation constant, while bandgaps are frequency bands with all propagation constants with non-zero imaginary part.

Computation of the forced harmonic response of the finite structure

At least two different approaches can be followed to compute the response due to a harmonic force using SEM. One can adopt the spectral transfer matrix method (STMM) (Lee, 2000), which reduces the complete structure to a single equivalent unit cell (represented by its TM) by recursively combining the TMs of the substructures that comprise the finite system. Although this approach is in principle exact and generates a linear system of low order (which is independent of number of unit cells), it is prone to numerical errors due to poor conditioning of the TM. Another approach, which is adopted here, consists of working directly with spectral element matrices. The DSM of the whole structure is assembled from the matrices of its constituent substructures using techniques completely analogous to those used in conventional FEM. Although the resulting system of equations may have a much higher order (which increases with the number of cells) when compared to that obtained when using STMM, the numerical problems described above are avoided.

The considered finite structure is composed of a set of $N - 1$ beam-type resonators, placed at a constant spacing along the host beam, which in turn is split into N segments. Thus, the equations of motions of the entire metamaterial beam can be written as:

$$\mathbf{S}\mathbf{d} = \mathbf{f}, \tag{25}$$

where the global DSM can be read as:

$$\mathbf{S} = \begin{bmatrix} \mathbf{S}_{11}^{(1)} & \mathbf{S}_{12}^{(1)} & \mathbf{0} & \cdots & \mathbf{0} & \mathbf{0} \\ \mathbf{S}_{21}^{(1)} & \mathbf{S}_{22}^{(1)} + \mathbf{S}_{11}^{(2)} + \mathbf{S}_{\mathrm{r}}^{(1)} & \mathbf{S}_{12}^{(2)} & \cdots & \mathbf{0} & \mathbf{0} \\ \mathbf{0} & \mathbf{S}_{21}^{(2)} & \mathbf{S}_{22}^{(2)} + \mathbf{S}_{11}^{(3)} + \mathbf{S}_{\mathrm{r}}^{(2)} & \cdots & \mathbf{0} & \mathbf{0} \\ \vdots & \vdots & \vdots & \ddots & \vdots & \vdots \\ \mathbf{0} & \mathbf{0} & \mathbf{0} & \cdots & \mathbf{S}_{22}^{(N-1)} + \mathbf{S}_{11}^{(N)} + \mathbf{S}_{\mathrm{r}}^{(N-1)} & \mathbf{S}_{12}^{(N)} \\ \mathbf{0} & \mathbf{0} & \mathbf{0} & \cdots & \mathbf{S}_{21}^{(N)} & \mathbf{S}_{22}^{(N)} \end{bmatrix}, \tag{26}$$

and the vectors of forces and nodal degrees of freedom can be represented as:

$$\mathbf{f} = \{Q_1 \quad 0 \quad \cdots \quad 0 \quad 0\}^{\mathrm{T}}, \qquad \mathbf{d} = \{W_1 \quad \Phi_1 \quad W_2 \quad \Phi_2 \quad \cdots \quad W_{N+1} \quad \Phi_{N+1}\}^{\mathrm{T}}. \tag{27}$$

Since we are concerned with the vibration attenuation performance of the system, a natural metric to evaluate it is the displacement transmissibility between the first (where the force is applied) and last nodes, which is given by:

$$T(\omega) = \left|\frac{W_{N+1}}{W_1}\right|. \tag{28}$$

NUMERICAL EXPERIMENTS AND DISCUSSION

The trade-off between vibration attenuation and its robustness in a finite metamaterial

In order to highlight the motivation behind this study, this section stresses the trade-off between the vibration attenuation obtained in a finite metamaterial and its robustness. Here, robustness is qualitatively understood as a small change in the displacement transmissibility (as defined in Eq. (28)) as the forcing frequency is slightly varied.

Figure 2 shows the displacement transmissibility for the metamaterial beam when 1, 7, and 14 resonators are distributed equidistantly and symmetrically along its length (without adding the copper sheet on the resonators). It can be seen that the frequency range in which vibration attenuation occurs increases as the number of resonators embedded into the beam increases. At the same time, it can be noticed that the increase in the number of resonators leads to a greater amount of natural frequencies within each pass-band. Accompanied by this increase, there seems to be a clustering of these natural frequencies around the boundaries of the bandgaps (Mace, 2014). This grouping leads to a decrease in the robustness of the metamaterial design, since in a narrow frequency range around the cutoff frequency of the pass-band, one can move from a region with high attenuation to a region with high vibration transmissibility.

This phenomenon can be understood through the modal density of the metamaterial, $n(\omega)$, which is defined as the expected number of modes per unit of frequency. For an one-dimensional system composed of N unit cells, it can be calculated using the phase-closure principle (Mead, 1975) and is approximately given by (Langley, 1994; Lyon and DeJong, 1995):

$$n(\omega) = NL/(\pi c_g) = (N/\pi)\partial\mu/\partial\omega, \tag{29}$$

where L is the length of each unit cell, and c_g is the group velocity. Equation (29) ignores the possible influence of boundary conditions on the modal density (Xie et al., 2004), which is non-zero even for simple ones (such as free, pinned or clamped) in the case of Timoshenko beams (Mei and Mace, 2005). Nonetheless, for systems comprised of many unit cells, the modal density is asymptotically independent of the boundary conditions (Finnveden, 2004), so their contributions can be neglected.

For periodic structures, the dispersion relation is symmetric around $\mu = 0$, and periodic in the k-space, obeying $\omega(\mu) = \omega(\mu + 2\pi n)$, with n being an integer. Due to this periodicity and symmetry, for the dispersion diagram to have a continuous slope, one must have $\partial\omega/\partial\mu = 0$ for $\mu = 0$ and $\mu = \pi$. Indeed, it can be seen that the dispersion diagram shown in Fig. 3 presents a vertical slope for these values of μ. It follows from Eq. (29) that the modal density is infinite at the bandgaps edge frequencies, which explains the clustering of natural frequencies around this region.

Figure 4 shows the modal density computed numerically for the metamaterial beam. Comparing it with Fig. 2(c), one can clearly see an accumulation of natural frequencies in regions with higher modal density. It is noteworthy that, for the Bragg bandgap, the modal density increases (to infinity) only in regions very close to the cutoff frequency, while for the locally resonant bandgaps, it presents a more accentuated increase in regions farther from the band edges. This explains why there is much more significant clustering of natural frequencies around the locally resonant bandgaps than around the Bragg bandgap (cf. Fig. 2(c)).

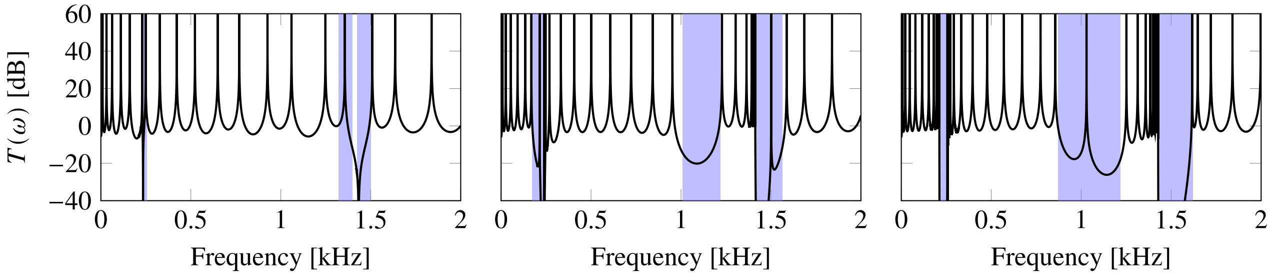

(a) 1 resonator (b) 7 resonators (c) 14 resonators

Figure 2 – Displacement transmissibility for a beam with (a) 1, (b) 7 and (c) 14 beam-type resonators. The blue hatched areas highlight the predicted bandgaps.

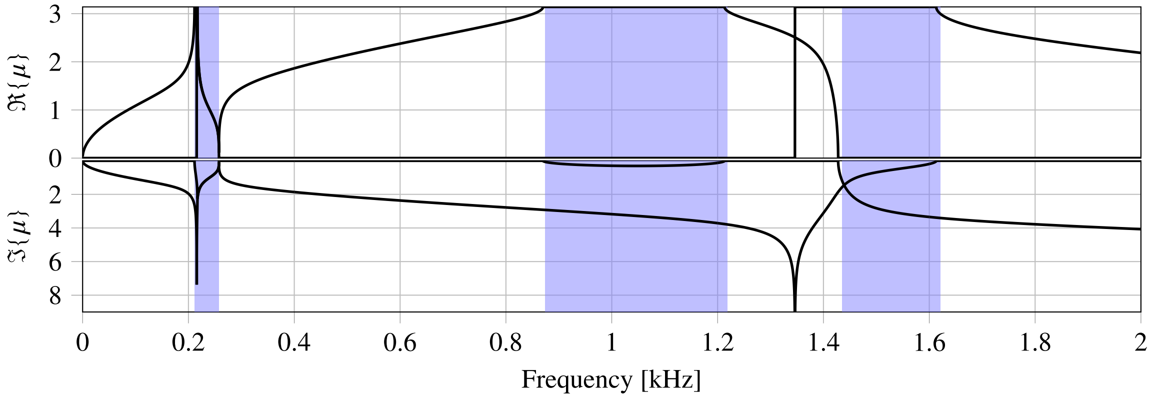

Figure 3 – Dispersion diagram for a beam with beam-type resonators. The associated unit cell is related to the structure whose transmissibility is shown in Fig. 2(c). The blue hatched areas highlight the predicted bandgaps.

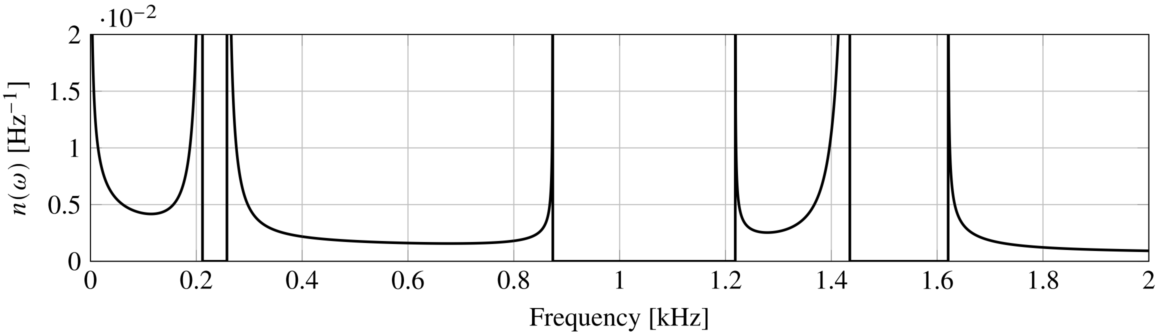

Figure 4 – Modal density for the metamaterial beam with 14 unit cells.

Exploiting eddy current damping in metamaterial beams with beam-type resonators

This section is devoted to showing how eddy current damping can be exploited to enhance the vibration attenuation performance of a metamaterial beam with beam-type resonators. The following case studies consider a metamaterial beam with 14 unit cells. The relevant geometric and material parameters are listed in Table 1. Complementary features are: permeability of free space, $\mu_0 = 4\pi \times 10^{-7}$ H/m; PM residual magnetic flux density, $B_r = 1.45$ T; PM length, $L_{\text{PM}} = 6.35$ mm; PM radius, $R_{\text{PM}} = 7.9375$ mm.

Using the previous parameters, the equivalent damping coefficient due to eddy currents, c_{EC}, can be computed using Eq. (7). Eddy currents generated in the aluminum resonator were also considered due to its high electrical conductivity. The variations of c_{EC} with x_{EC} (the position of the ECD along the length of the resonator) and z_{EC} (the separation between the conductive copper sheet and the surface of the PM) are shown in Fig. 5. The axes are normalized following $\bar{x} = (x_{\text{EC}} - b_r/2)/(L_r - b_r)$ (so that $0 \leq \bar{x} \leq 1$) and $\bar{z} = z_{\text{EC}}/L_{\text{PM}}$ (so that $0 < \bar{z} \leq 2$). It can be noticed that the damping coefficient decreases rapidly as the PM is distanced from the resonant structure. Much lower sensitivity is found concerning the ECD location along the resonator's length. For a given $\bar{z}$, c_{EC} reaches its maximum value at $x = 0.5$ and minimum values at $\bar{x} = 0$ and $\bar{x} = 1$.

The impact of eddy current damping on the wave attenuation performance of the LR metamaterial can be seen through the plot of the smallest attenuation constant as a function of frequency, since it characterizes the least spatially attenuated

Table 1 – Geometric and materials parameters of the unit cell of the metamaterial beam.

Feature	Host Beam	Beam-type resonator	Copper sheet
Length [m]	1.33	0.11	0.015875
Width [mm]	25.4	15.875	15.875
Thickness [mm]	4.7625	3.175	0.5
Mass density [kg/m^3]	2700	2700	8940
Young's modulus [MPa]	70	70	-
Poisson's ratio	0.33	0.33	-
Electrical conductivity [kS/mm]	36.9	36.9	58.7

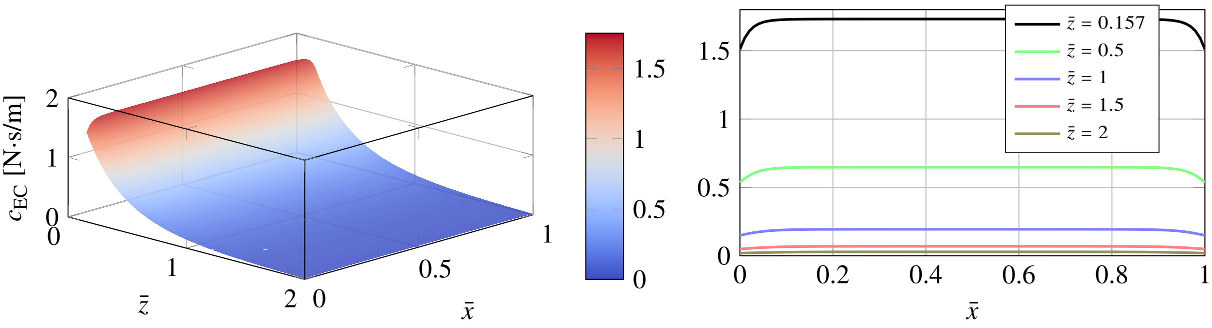

Figure 5 – Damping coefficient as a function of the location of the ECD.

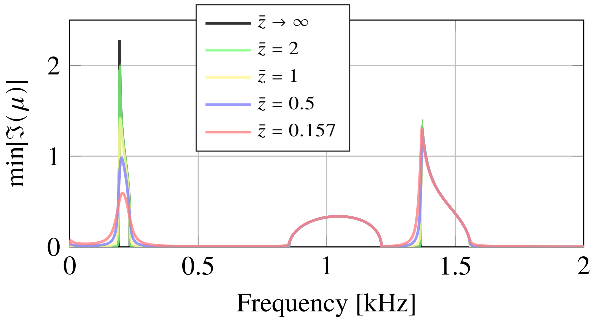

Figure 6 – Smaller attenuation constant for the LR metamaterial for different values of $\bar{z}$, when $\bar{x} = 1$.

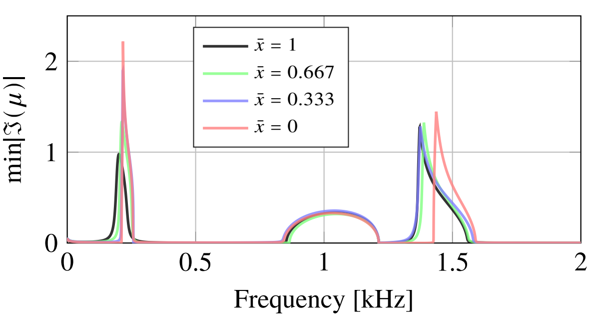

Figure 7 – Smaller attenuation constant for the LR metamaterial for different values of $\bar{x}$, when $\bar{z} = 0.5$.

wave mode (Xiao et al., 2013). This is shown in Fig. 6 when $\bar{x} = 1$ (i.e., the ECD is at the free end of the resonator) for different values of $\bar{z}$. It can be noticed that the addition of ECD mainly affects the frequency ranges closer to the boundaries of the LR bandgaps. For all levels of damping, the Bragg bandgap is almost unaffected, nor are the regions far from the bandgaps edge frequencies. For the bandgap associated with the first natural frequency of the resonator, the increase in attenuation bandwidth comes at the cost of decreasing the maximum achieved attenuation. For the second natural frequency, this bandwidth increases without substantially affecting the value of the smallest attenuation constant.

The influence of varying the ECD insertion point, $\bar{x}$, on the smallest attenuation constant can be seen in Fig. 7 when $\bar{z} = 0.5$. It is noticed that the center frequency of the attenuation bands decreases as the ECD moves from $\bar{x} = 0$ to $\bar{x} = 1$. The Bragg bandgap, in turn, remains almost unchanged. It is also interesting to note that the location $\bar{x} = 1$ is the one that promotes a greater width of the attenuation band for the first LR bandgap. As the ECD moves to the coupling point on the beam, the damping effects become less pronounced in this frequency region. Regarding the second LR bandgap, the attenuation range becomes wider when $\bar{x} = 0.333$ (for the four cases considered). For both LR bandgaps, the point $\bar{x} = 0$ is the one that most suppresses the effects of ECD.

Similar trends can be observed regarding the vibration attenuation achieved in a finite structure. Figures 8 and 9 show the vibration transmissibility for different values of $\bar{z}$ when $\bar{x} = 1$. They reveal that, although ECD reduces the vibration transmissibility of all natural frequencies, it is particularly effective regarding those clustered close to the cutoff frequencies of the LR bandgaps. Figure 9 shows that natural frequencies away from this region, as well as those within the Bragg bandgap, are much less attenuated, even for higher damping levels. It is worth noting that the placement position $\bar{x} = 1$ is

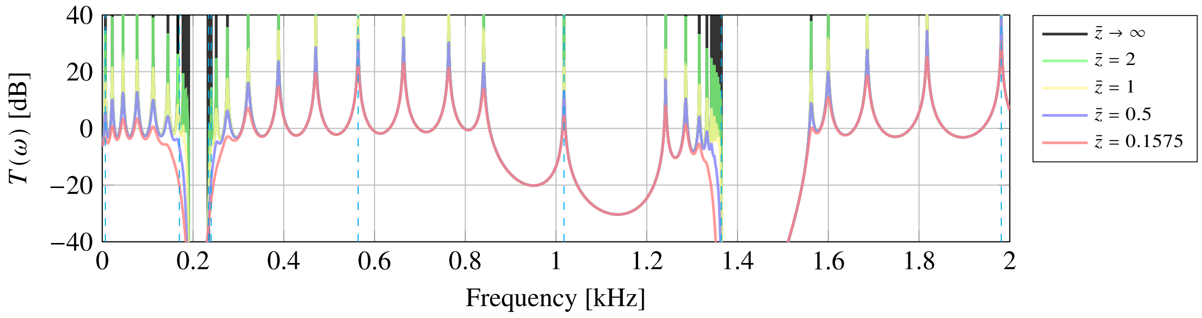

Figure 8 – $T(\omega)$ for the LR metamaterial for different values of $\bar{z}$, when $\bar{x} = 1$.

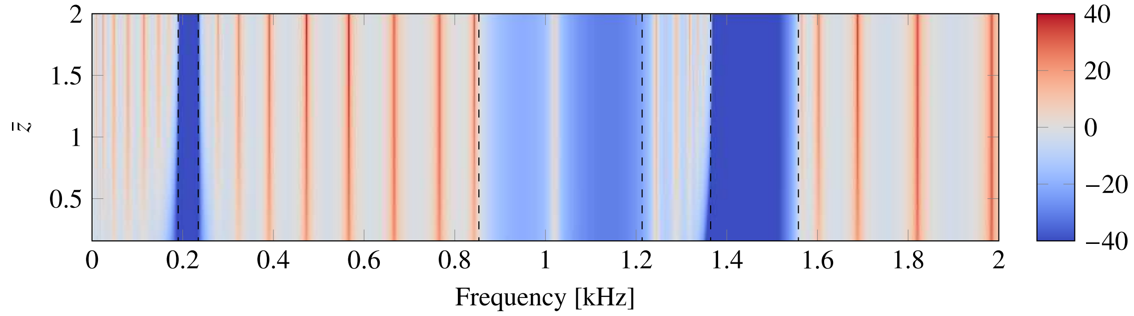

Figure 9 – $T(\omega)$ **in dB for the LR metamaterial for different values of** $\bar{z}$**, when** $\bar{x} = 1$**. The dashed lines represent the predicted bandgaps.**

capable to attenuate the modes close to both LR bandgaps. Although Fig. 6 shows that the maximum attenuation obtained in the region of the first LR bandgap decreases as the damping level increases, this effect cannot be observed in Figs. 8 and 9. Indeed, for all damping levels assumed, the vibration transmissibility within the first LR bandgap is always below the considered limit of −40 dB. This is due to the relatively large number of unit cells that comprise the finite structure.

Concerning the ECD insertion point, $\bar{x}$, the conclusions obtained through the wave propagation analysis are also reflected in the vibration transmissibility of the finite structure. Figures 10 and 11 show the vibration transmissibility for different values of $\bar{x}$ when $\bar{z} = 0.5$. In the frequency regions around the first LR bandgap, the maximum attenuation is obtained for $\bar{x} = 1$. As the ECD coupling point moves to $\bar{x} = 0$, the modes clustered in this region become less and less attenuated. For modes close to the cutoff frequencies of the second LR bandgap, Fig. 11 shows that the maximum attenuation is obtained for about $\bar{x} = 0.45$.

To help understand the influence of the ECD coupling point on attenuation performance, Fig. 12 shows the normal modes for 8 natural frequencies when $\bar{x} = 1$. The corresponding frequencies are shown as dashed blue lines in Fig. 8. It can be noticed that the natural frequencies that are far from the bandgaps regions present a deformation pattern with large deformation of the host beam, whereas there may be large deformations of the resonators (as in Figs. 12(e) and 12(g)) or not (cf. Fig. 12(a)). In these cases, the localized use of the ECD in the resonator is not very effective, as the host beam possesses regions with large displacements which are not directly damped. The modes close to the LR bandgaps (Figs. 12(b), 12(c), 12(d), and 12(g)) are dominated by deformations of the resonators in configurations close to their respective

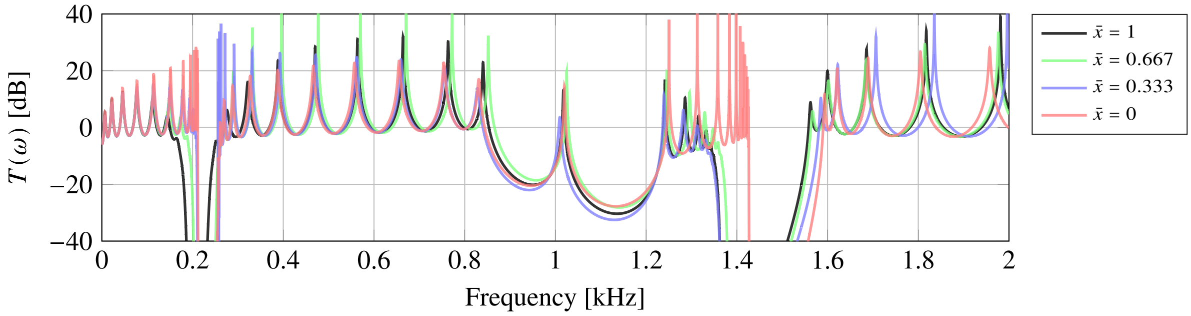

Figure 10 – $T(\omega)$ **for the LR metamaterial for different values of** $\bar{x}$**, when** $\bar{z} = 0.5$**.**

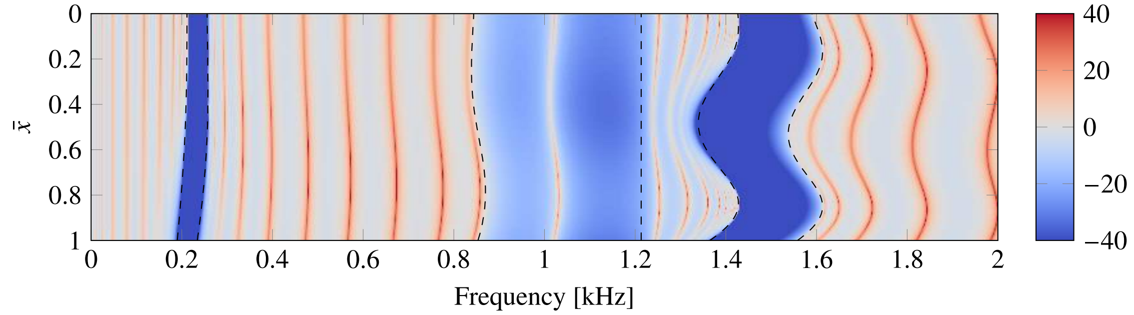

Figure 11 – $T(\omega)$ **in dB for the LR metamaterial for different values of** $\bar{x}$**, when** $\bar{z} = 0.5$**. The dashed lines represent the predicted bandgaps.**

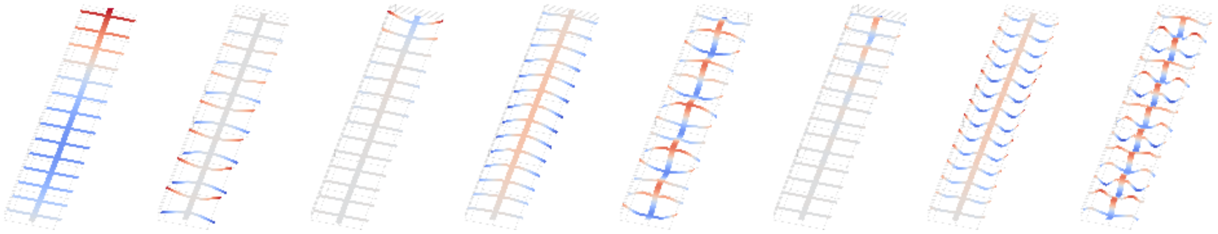
(a) 6.81 Hz (b) 189.96 Hz (c) 233.08 Hz (d) 234.13 Hz (e) 563.79 Hz (f) 1017.56 Hz (g) 1364.32 Hz (h) 1981.26 Hz

Figure 12 – Some normal modes for the metamaterial beam when $\bar{x} = 1$.

normal mode, with small deformations of the host beam. In these cases, the localized use of the ECD in the resonators is quite effective. From Fig. 12(f), it can be seen that the deformation mode for the natural frequency within the Bragg bandgap corresponds to a localized vibration mainly of the host beam, which explains the low effectiveness of the ECD for attenuating this mode. Comparing Figs. 12(b) and 12(g), one can understand the influence of the ECD location on the frequency range that is more attenuated. For frequencies close to the first LR bandgap, the regions of the structure with the greatest displacements (and therefore the greatest velocities and, hence, damping force) are at the free ends of the resonators. This remains true for the normal modes of all natural frequencies that are clustered close to the first LR bandgap. Therefore, when the ECD is located near the free extremity of the resonator, it is able to improve the structure's vibration transmissibility performance, as seen in Figs. 8 and 9. A similar analysis explains the attenuation close to the second LR bandgap.

CONCLUSION

This paper considered the use of the eddy current damping mechanism to improve the vibration performance of metamaterial beams composed of a host beam with beam-type resonators. It has been shown how increasing the number of considered unit cells in a finite structure enhances the transmissibility attenuation, but also increases the number of natural frequencies within a given branch of the dispersion diagram. Furthermore, it has been shown that these natural frequencies tend to accumulate close to the cut-off frequencies of the dispersion diagram, which leads to a loss of robustness of the structure. Finally, it was shown how eddy current damping, when inserted into the resonating structure, can be used to reduce this lack of robustness. The influence of the position of the EC damper along the resonator, as well as the amount of damping, on the attenuation performance was investigated in terms of both the dispersion diagram and the displacement transmissibility. The obtained results show that eddy current damping can be used to improve the vibration attenuation of metamaterial beams with beam-type resonators.

ACKNOWLEDGMENTS

M. B. R. Fernandes is grateful to the São Paulo State Research Foundation (FAPESP) for his doctorate scholarship (grant #2019/19921-5). All authors also acknowledge FAPESP for supporting their work through a thematic grant (Periodic structure design and optimization for enhanced vibroacoustic performance: ENVIBRO, #2018/15894-0). D. A. Rade acknowledges the Brazilian National Council for Scientific and Technological Development (CNPq) for the financial support to his research work (grant #312068/2020-4).

REFERENCES

Aladwani, A. and Nouh, M., 2020a, "Mechanics of metadamping in flexural dissipative metamaterials: Analysis and design in frequency and time domains", International Journal of Mechanical Sciences, Vol. 173, p. 105459.

Aladwani, A. and Nouh, M., 2020b, "Strategic Damping Placement in Viscoelastic Bandgap Structures: Dissecting the Metadamping Phenomenon in Multiresonator Metamaterials", Journal of Applied Mechanics, Vol. 88, No. 2.

Andreassen, E. and Jensen, J.S., 2013, "Analysis of Phononic Bandgap Structures With Dissipation", Journal of Vibration and Acoustics, Vol. 135, No. 4.

Ao, W.K. and Reynolds, P., 2019, "Evaluation of eddy current damper for vibration control of a frame structure", Journal of Physics Communications, Vol. 3, No. 5, p. 055013.

Bae, J.S., Park, J.S., Hwang, J.H., Roh, J.H., do Pyeon, B. and Kim, J.H., 2018, "Vibration Suppression of a Cantilever Plate Using Magnetically Multimode Tuned Mass Dampers", Shock and Vibration, Vol. 2018, pp. 1–13.

Belle, L.V., Claeys, C., Deckers, E. and Desmet, W., 2017, "On the impact of damping on the dispersion curves of a locally resonant metamaterial: Modelling and experimental validation", Journal of Sound and Vibration, Vol. 409, pp. 1–23.

Cheng, Y., Xu, J.Y. and Liu, X.J., 2008, "One-dimensional structured ultrasonic metamaterials with simultaneously negative dynamic density and modulus", Physical Review B, Vol. 77, No. 4.

El-Borgi, S., Fernandes, R., Rajendran, P., Yazbeck, R., Boyd, J. and Lagoudas, D., 2020, "Multiple bandgap formation in a locally resonant linear metamaterial beam: Theory and experiments", Journal of Sound and Vibration, Vol. 488, p. 115647.

Finnveden, S., 2004, "Evaluation of modal density and group velocity by a finite element method", Journal of Sound and Vibration, Vol. 273, No. 1-2, pp. 51–75.

Frazier, M.J. and Hussein, M.I., 2016, "Generalized Bloch's theorem for viscous metamaterials: Dispersion and effective properties based on frequencies and wavenumbers that are simultaneously complex", Comptes Rendus Physique, Vol. 17, No. 5, pp. 565–577.

Hussein, M.I. and Frazier, M.J., 2013, "Metadamping: An emergent phenomenon in dissipative metamaterials", Journal of Sound and Vibration, Vol. 332, No. 20, pp. 4767–4774.

Hussein, M.I., Leamy, M.J. and Ruzzene, M., 2014, "Dynamics of Phononic Materials and Structures: Historical Origins, Recent Progress, and Future Outlook", Applied Mechanics Reviews, Vol. 66, No. 4.

Laborenz, J., Krack, M., Panning, L., Wallaschek, J., Denk, M. and Masserey, P.A., 2012, "Eddy Current Damper for Turbine Blading: Electromagnetic Finite Element Analysis and Measurement Results", Journal of Engineering for Gas Turbines and Power, Vol. 134, No. 4.

Langley, R., 1994, "On the Modal Density and Energy Flow Characteristics of Periodic Structures", Journal of Sound and Vibration, Vol. 172, No. 4, pp. 491–511.

Lee, U., 2000, "Vibration analysis of one-dimensional structures using the spectral transfer matrix method", Engineering Structures, Vol. 22, No. 6, pp. 681–690, ISSN 0141-0296.

Lee, U., 2009, "Spectral Element Method in Structural Dynamics", Wiley, ISBN 9780470823750.

Liu, Z., Zhang, X., Mao, Y., Zhu, Y.Y., Yang, Z., Chan, C.T. and Sheng, P., 2000, "Locally Resonant Sonic Materials", Science, Vol. 289, No. 5485, pp. 1734–1736.

Lou, J., He, L., Yang, J., Kitipornchai, S. and Wu, H., 2018, "Wave propagation in viscoelastic phononic crystal rods with internal resonators", Applied Acoustics, Vol. 141, pp. 382–392.

Lyon, R. and DeJong, R., 1995, "Theory and Application of Statistical Energy Analysis", Butterworth-Heinemann, ISBN 9780750691116.

Mace, B.R., 2014, "Discussion of "Dynamics of Phononic Materials and Structures: Historical Origins, Recent Progress and Future Outlook" (Hussein, M. I., Leamy, M. J., and Ruzzene, M., 2014, ASME Appl. Mech. Rev., 66(4), p. 040802)", Applied Mechanics Reviews, Vol. 66, No. 4.

Mead, D., 1975, "Wave propagation and natural modes in periodic systems: II. Multi-coupled systems, with and without damping", Journal of Sound and Vibration, Vol. 40, No. 1, pp. 19–39.

Mei, C. and Mace, B.R., 2005, "Wave Reflection and Transmission in Timoshenko Beams and Wave Analysis of Timoshenko Beam Structures", Journal of Vibration and Acoustics, Vol. 127, No. 4, pp. 382–394, ISSN 1048-9002.

Ravaud, R., Lemarquand, G., Babic, S., Lemarquand, V. and Akyel, C., 2010, "Cylindrical Magnets and Coils: Fields, Forces, and Inductances", IEEE Transactions on Magnetics, Vol. 46, No. 9, pp. 3585–3590.

Serrano, Ó., Zaera, R. and Fernández-Sáez, J., 2019, "On the Mechanism of Bandgap Formation in Beams With Periodic Arrangement of Beam-Like Resonators", Journal of Vibration and Acoustics, Vol. 141, No. 6.

Sodano, H.A., Bae, J.S., Inman, D.J. and Belvin, W.K., 2005, "Concept and model of eddy current damper for vibration suppression of a beam", Journal of Sound and Vibration, Vol. 288, No. 4-5, pp. 1177–1196.

Sodano, H.A., Bae, J.S., Inman, D.J. and Belvin, W.K., 2006, "Improved Concept and Model of Eddy Current Damper", Journal of Vibration and Acoustics, Vol. 128, No. 3, pp. 294–302.

Xiao, Y., Wen, J., Wang, G. and Wen, X., 2013, "Theoretical and Experimental Study of Locally Resonant and Bragg Band Gaps in Flexural Beams Carrying Periodic Arrays of Beam-Like Resonators", Journal of Vibration and Acoustics, Vol. 135, No. 4.

Xie, G., Thompson, D. and Jones, C., 2004, "Mode count and modal density of structural systems: relationships with boundary conditions", Journal of Sound and Vibration, Vol. 274, No. 3-5, pp. 621–651.

Yao, S., Zhou, X. and Hu, G., 2008, "Experimental study on negative effective mass in a 1D mass–spring system", New Journal of Physics, Vol. 10, No. 4, p. 043020.

RESPONSIBILITY NOTICE

The authors are the only responsible for the printed material included in this paper.